

Revealing the mechanisms of NH₃ adsorption and reactions in catalytic NO_x reduction over Cu_x/CHA zeolites by in situ DRIFTS spectroscopy

Yali Shen^a, Zhiqiang Wang^b, Shasha Ge^a, Li Wang^a, Wangcheng Zhan^a, Qiguang Dai^a, Yanglong Guo^a, Yun Guo^{a,*}, Aiyong Wang^{a,*}

^a State Key Laboratory of Green Chemical Engineering and Industrial Catalysis, Research Institute of Industrial Catalysis, School of Chemistry and Molecular Engineering, East China University of Science and Technology, Shanghai 200237, PR China

^b State Key Laboratory of Green Chemical Engineering and Industrial Catalysis, Centre for Computational Chemistry and Research Institute of Industrial Catalysis, School of Chemistry and Molecular Engineering, East China University of Science and Technology, Shanghai 200237, PR China

ARTICLE INFO

Keywords:
NH₃-SCR
Cu-SSZ-13
NH₃ solvation
Intra-zeolite oxolation

ABSTRACT

Adsorption and activation of NH₃ on Cu-SSZ-13 were essential for NO_x removal, however, their important role at the molecular level remains unclear. In this work, the Al-rich Cu/SSZ-13 (Cu_x/CHA) catalysts were synthesized by the incipient-wetness impregnation method, and the NH₃-SCR performance was investigated. It is found that high Cu content promoted the formation of Z-[Cu(OH)]⁺ and CuO_x particles, enhanced the adsorption capacity of NO_x, and increased the intra-zeolite oxolation process in the Cu_x/CHA catalysts. *In situ* DRIFTS results showed that the Z-[Cu(OH)(NH₃)_x]⁺(x<3) exhibited analogous properties to B-NH₄⁺, but it would convert to Z-[Cu(OH)(NH₃)₃]⁺ with increasing NH₃ adsorption time and exhibit L-NH₃ properties. Those findings could provide a new insight into understanding the adsorption and activation of NH₃ in low-temperature reactions, as well as new ideas for improving NO_x conversion during cold start.

1. Introduction

Nitrogen oxides (NO_x) are characteristic pollutants of diesel vehicle exhaust emissions, and NH₃ selective catalytic reduction (NH₃-SCR) has been recognized as the most widely used and effective method for NO_x emission control [1,2]. Recently, small-pore Cu-SSZ-13 catalyst, with CHA structure, have excellent NH₃-SCR catalytic performance in the range of 200–450 °C and have been widely investigated as mainstream NH₃-SCR catalysts [3–5]. However, the low performance below 200 °C does not ensure effective NO_x removal under cold-start conditions [6]. Therefore, studies on the NO_x reduction mechanism of Cu-SSZ-13 catalysts provide theoretical support for better understanding and design of catalysts with excellent low-temperature NH₃-SCR catalytic performance.

Isolated Cu^{II} ions and CuO_x are the main forms of Cu species existed in Cu-SSZ-13, in which two types of isolated Cu^{II} ions exist, one is Z₂-Cu²⁺ located in the double 6-membered ring position (Z represents the framework Al), and the other is Z-[Cu(OH)]⁺ located in the 8-membered ring position [7–9]. In earlier studies, it was suggested that Z-[Cu(OH)]⁺ occurred only when Z₂-Cu²⁺ was fully saturated because Z₂-Cu²⁺ was

thermodynamically more stable than Z-[Cu(OH)]⁺ [10,11]. With further research, Z-[Cu(OH)]⁺ was found to be formed along with Z₂-Cu²⁺ due to kinetic stabilization effects during the ion exchange process [12]. Furthermore, the synthesis method [13], Cu content [14], and Si/Al ratio [14] of the zeolite will affect the distribution of Cu species (i.e., Z-[Cu(OH)]⁺, Z₂-Cu²⁺, and CuO_x) in Cu-SSZ-13.

In the case of the standard SCR reaction on Cu-SSZ-13 zeolite, active site evolution consists mainly of two half-cycle reactions, i.e., reduction cycle (Cu²⁺→Cu⁺) and oxidation cycle (Cu⁺→Cu²⁺) [9,15–17]. It has been found that the NH₃-SCR reaction exhibited different reaction mechanisms in the lower and higher temperature regions [18]. The active site in the lower temperature range is dynamically changing and dominated by transient Cu dimer formed by NH₃-dissolved [Cu^I(NH₃)₂]⁺ species [19–21], whereas the active site in the high-temperature region is an isolated Cu^{II} ionic site [18]. In addition, the researcher also found that Z-[Cu(OH)]⁺ exhibited higher activity than Z₂-Cu²⁺ in both reduction by NH₃ and oxidation to bidentate nitrate by NO [22]. Lee et al. [23] found that Z-[Cu(OH)]⁺ species had higher mobility and were more readily diffusible than the Z₂-Cu²⁺ species during the forming of the dimerized Cu intermediates (i.e.,

* Corresponding authors.

E-mail addresses: yunguo@ecust.edu.cn (Y. Guo), wangaiyong@ecust.edu.cn (A. Wang).



$[\text{Cu}^{\text{I}}(\text{NH}_3)_2]^+$ -O₂-[Cu^I(NH₃)₂]⁺), resulting in higher reactivity properties. Thus, the NH₃-SCR activity in the low-temperature region correlated mainly with Z-[Cu(OH)]⁺ species after NH₃ solvation.

The NH₃ solvation process was very important for the low-temperature NH₃-SCR performance. It has been shown that the existence of H₂O and NH₃ affected the coordinating environment of Cu species in Cu-SSZ-13 catalyst at temperatures below 250 °C [9]. In the existence of H₂O, Cu species form hydrated Cu complexes, whereas when NH₃ was present, NH₃ preferentially adsorbs Cu species within the Cu-SSZ-13 zeolites to form mobile Cu-amine complexes, leading to higher mobility [9,24]. For isolated Cu^{II} ions on Cu-SSZ-13 (Z₂-Cu²⁺ and Z-[Cu(OH)]⁺), with introducing NH₃ species, it is possible to generate Z₂-[Cu(NH₃)₂]²⁺, Z₂-[Cu(NH₃)₂]²⁺, Z₂-[Cu(NH₃)₃]²⁺, Z-[Cu(OH)NH₃]⁺, Z-[Cu(OH)(NH₃)₂]⁺, and Z-[Cu(OH)(NH₃)₃]⁺ species [1,22,24,25]. In fact, the generation of Cu-amine complexes weakened the interaction between isolated Cu^{II} ions and the zeolite framework and increased the mobility of isolated Cu^{II} ions, which allowed the NH₃-solvated Cu ions to form Cu dimers inside or across the zeolite cage, and thus to be involved in the NH₃-SCR catalytic reactions in the low-temperature region. However, theoretical calculations suggested that linear [Cu^I(NH₃)₂]⁺ was more mobile, but as noted above, no change in valence of the isolated Cu^{II} ions was observed during NH₃ solvation process, thus requiring reaction with NO to generate linear [Cu^I(NH₃)₂]⁺ species, which in turn reacts with O₂ to generate [Cu^I(NH₃)₂]⁺-O₂-[Cu^I(NH₃)₂]⁺ intermediates [26].

Moreover, there was controversy over the number of NH₃ coordination sites for the isolated Cu^{II} ion on Cu-SSZ-13, with some scholars suggesting that the Z₂-Cu²⁺ site was coordinated to a maximum of two NH₃, whereas the Z-[Cu(OH)]⁺ site was coordinated to a maximum of one NH₃ [19]. In contrast, some scholars suggested that isolated Cu^I ions would dissolve with two NH₃ ligands to form linear Cu^I(NH₃)₂, while the isolated Cu^{II} ion would form a four-coordination complex with four or three NH₃, i.e., Z₂-[Cu(NH₃)₄]²⁺ and Z-[Cu(OH)(NH₃)₃]⁺ [8,18]. Although the NH₃ solvation process of Cu species on Cu-SSZ-13 has been investigated, however, the relevant properties exhibited by the NH₃ solvation process need to be further investigated.

In this paper, a series of aluminum-rich Cu_x/SSZ-13 (Cu_x/CHA) were prepared by using the incipient-wetness impregnation technique. The relationship between Cu²⁺ sites and reaction performance in Cu_x/CHA was also established by combining XRD Rietveld refinement, structural characterization, redox property characterization and in situ spectroscopic analysis. In addition, the NH₃ solvation process and reaction mechanism on Cu_x/CHA with different contents of Z₂-Cu²⁺, Z-[Cu(OH)]⁺ and CuO_x species were investigated by *in situ* DRIFTS.

2. Experimental

2.1. Catalysts preparation

Cu-SSZ-13 catalysts with different Cu content were synthesized by incipient-wetness impregnation (IWI) from commercially available H-SSZ-13 zeolites. Briefly, the needed dosage of Cu(NO₃)₂·3 H₂O was first diluted with H₂O and then mixed with 2 g H-SSZ-13, ultrasonicated for 20 min, dried overnight at 110 °C, followed by calcination for 4 h at 550 °C in static air. The resulting powder was expressed as Cu_x/CHA, in which x is the actual copper content in the catalyst obtained by ICP-OES.

2.2. Characterization

The species, location and distribution properties of Cu species in Cu_x/CHA were investigated by various characterization methods, such as ICP-OES, N₂ adsorption-desorption analysis, XRD, HAADF-STEM, H₂-TPR, UV-vis, NO_x-TPD, and NH₃-TPD, the specific test conditions were the same as in previous studies [27,28], see Supporting information.

The NH₃ solvation process and reaction mechanism on Cu_x/CHA were investigated by *in situ* DRIFTS (Nicolet Nexus 6700 FT-IR

spectrometer), as described in the Supporting information.

2.3. Catalytic performance

A NO_x chemiluminescence analyzer (Thermo Fisher Model 42i-HL) and a Nicolet 6700 FT-IR spectrometer were used to investigate the NO conversion, N₂ selectivity and N₂O concentration of Cu_x/CHA. The feed gas contained 500 ppm NH₃, 500 ppm NO, 5 vol% O₂, 5 vol% H₂O, and was equilibrated with Ar at a weight hourly space velocity (WHSV) of 180,000 mL·h⁻¹ g⁻¹. Tests details on the NH₃-SCR activity and kinetics of Cu_x/CHA were given in the Supporting information.

3. Results and discussion

3.1. Structural properties

3.1.1. XRD

The XRD spectra of Cu_x/CHA are presented in Fig. 1(a) and S1, all samples showed a typical CHA framework structure. No diffraction peaks of Cu-related species (such as CuO (PDF# 48-1548), CuAl₂O₄ (PDF# 33-0448), and CuAlO₂ (PDF# 35-1401)) were observed on Cu_x/CHA, suggesting that the Cu species were dispersed highly in SSZ-13, or the particles size was smaller than the XRD limit of detection [27]. Moreover, the ratio of the peak intensity of (101) and (211) ($I_{(101)}/I_{(211)}$) was decreased with the increase of Cu content (Fig. 1(b)). The decreased $I_{(101)}/I_{(211)}$ could correspond to the Cu species in Cu_x/CHA, the existence of which in the 8-membered ring (Z-[Cu(OH)]⁺) caused a certain amount of deformation of the zeolite framework structure, thus reducing the reflectivity of the (101) crystal surface [29]. Therefore, the higher the copper content, the more Z-[Cu(OH)]⁺ species close to the position of the 8-membered ring, and the more pronounced the resulting deformation.

The Rietveld refinement of H-SSZ-13(CHA) was first performed, and the result is shown in Figs. S1(a) and S2. As shown in Fig. S2, H-SSZ-13 (CHA) had a typical CHA structure, which mainly consisted of the 8-membered ring (8MR), 6-membered ring (6MR), and 4-membered ring (4MR) structures. Then, the Rietveld refinement of copper-containing zeolites (Cu_x/CHA) was carried out by using the refined H-SSZ-13 structure as the initial model as in previous studies [27], and the results are illustrated in Fig. 1(d) and S1(b-e).

The positions of Cu₁ (located in 6MR, coordinated to three oxygen atoms of the 6MRs, named as Z₂-Cu²⁺) and Cu₂ (located in the chabazite cage nearby 8MR, named as Z-[Cu(OH)]⁺) in Cu_x/CHA are illustrated in Fig. 1(e). As demonstrated in Table S1 and Fig. 1(c), with increasing Cu content, the OCC_{Cu1} (the occupancies of Cu₁) in Cu_x/CHA increased significantly firstly and then slightly changed when the Cu content was higher than 3.8 wt%. At the same time, the OCC_{Cu2} (occupancies of Cu₂) in Cu_x/CHA increased monotonically with increasing Cu content. These results suggested that more Cu species occupied the ion-exchange sites of zeolites as increasing Cu content and that Z₂-Cu²⁺ could be saturated when the copper content was higher than 3.8 wt%.

3.1.2. N₂ adsorption-desorption analysis

BET surface areas (S_{BET}) and pore volumes (V_{pore}) of Cu_x/CHA are summarized in Table S2 and Fig. S3. The S_{BET} and V_{pore} of Cu_x/CHA decreased with increasing copper content, which could be due to the blocking of zeolite pores by Cu ions entering into the pores, thus decreasing the S_{BET} and V_{pore} of Cu_x/CHA, and the higher the Cu content, the more significant the effect.

3.1.3. STEM and EDS

The structure and elemental distribution of Cu_x/CHA were carried out by HAADF-STEM and EDS mapping (Fig. 2). For Cu_{0.97}/CHA, Cu was highly dispersed (Fig. 2(a)). More Cu was found in Cu_{1.9}/CHA (Fig. 2(b)) and highly dispersed. Further increasing the Cu content to 4.7 wt%, most of the copper was highly dispersed in the Cu_{4.7}/CHA zeolite,

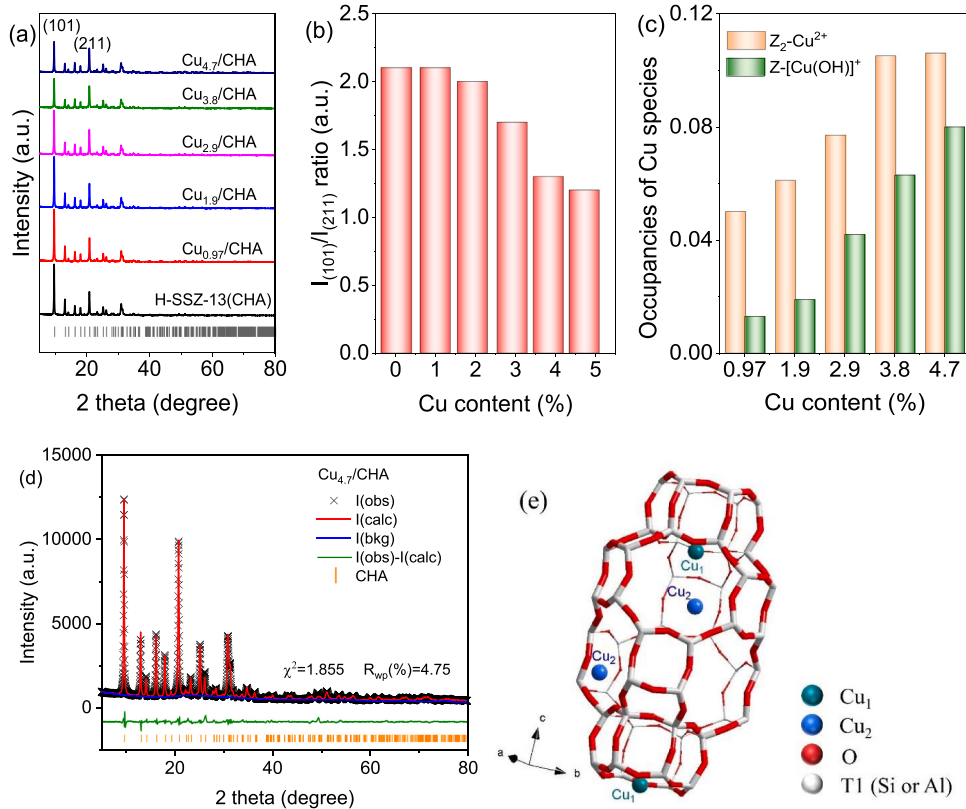


Fig. 1. (a) XRD patterns of Cu_x/CHA catalyst; (b) The ratio of I₍₁₀₁₎ / I₍₂₁₁₎ obtained by (a); (c) The occupancies of Cu species; (d) XRD pattern and calculated Rietveld refinement pattern of Cu_{4.7}/CHA. (e) Structural models of Cu_x/CHA samples. (Cu₁: located in 6MR, coordinated to three oxygen atoms of the 6MRs, such as Z₂-Cu²⁺; Cu₂: located in the chabazite cage, such as Z-[Cu(OH)]⁺ in 8MR).

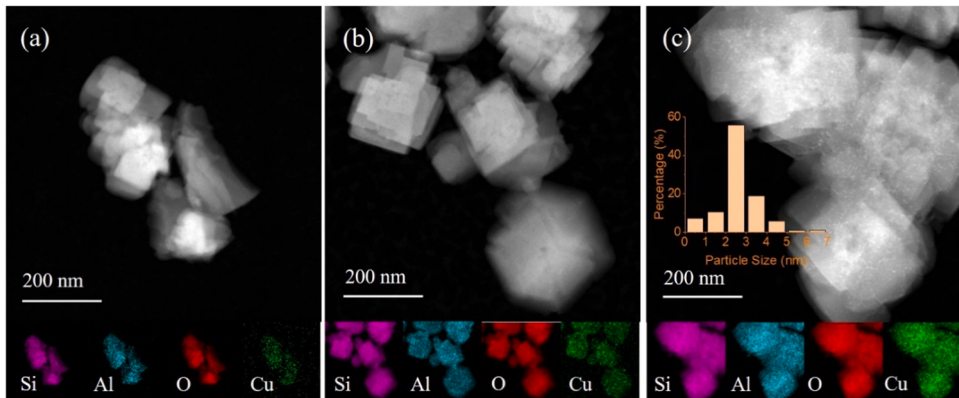


Fig. 2. STEM-EDS mappings of (a) Cu_{0.97}/CHA, (b) Cu_{1.9}/CHA, (c) Cu_{4.7}/CHA.

however, a small amount of copper was present as CuO_x particles with a mean particle diameter of 2.3 nm, as shown as Fig. 3(c). Those results indicated that low contents could be well dispersed in the zeolite, while Cu species could agglomerate to produce CuO_x species when the copper content was too high.

3.2. Distribution of different Cu species

3.2.1. H₂-TPR

The reducible properties of Cu_x/CHA were further investigated by H₂-TPR testing as illustrated in Fig. 3 and S4. Of note, there was no H₂ consuming peak observed in H-SSZ-13(CHA) (Fig. S4), demonstrated that all the H₂ consuming peaks in the H₂-TPR curves of Cu_x/CHA originated from the Cu species reduction. The H₂ consuming peaks of

Cu_x/CHA (Fig. 3) could be decomposed into four peaks (A, B, C, and D). Peak B (283 °C) was ascribed to the reduction of CuO_x particles (Cu²⁺ → Cu⁰) [27]. Peak A (234 °C) and peak C (338 °C) were attributed to the reduction of isolated Cu²⁺ ions (Z-[Cu(OH)]⁺ and Z₂-Cu²⁺) to isolated Cu⁺ ions, respectively [30,31]. And peak D (> 500 °C) was assigned to the further reduction of isolated Cu⁺ (Cu⁺ → Cu⁰) [32].

The contents of different Cu species in the Cu_x/CHA catalysts were calculated according to H₂-TPR, and summarized in Fig. 3(b) and S5. Fig. 3(b) showed that the amount of Z-[Cu(OH)]⁺ and CuO_x (calculated by H₂-TPR) in the Cu_x/CHA increased remarkably with the increase of Cu content (obtained by ICP-OES). However, the amount of Z₂-Cu²⁺ in the Cu_x/CHA increased remarkably with the increase of Cu content from 0.97 wt% to 3.8 wt%, but did not change significantly when the copper content was higher than 3.8 wt%. Those results were also verified in the

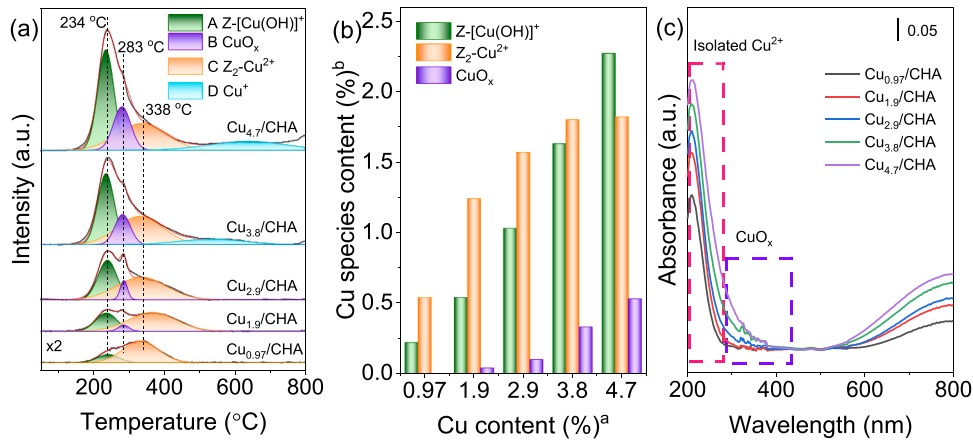


Fig. 3. (a) H₂-TPR profiles of Cu_x/CHA catalysts, and their deconvolved results (b) of Cu_x/CHA catalysts; (c) UV-vis spectroscopy of Cu_x/CHA catalysts. ^a: Obtained by ICP-OES. ^b: Calculated from hydrogen consumption peaks below 500 °C.

results of XRD Rietveld refinement and HAADF-STEM, which was probably resulted from the limited amount of 6MR sites in the CHA zeolite, leading to an easier generation of CuO_x and Z-[Cu(OH)]⁺ species at high Cu contents. In addition, Fig. S5 showed that the Z₂-Cu²⁺ species percentage decreased with increasing Cu content, while the CuO_x and Z-[Cu(OH)]⁺ species percentage increased. These results suggested that

high Cu content promoted the formation of Z-[Cu(OH)]⁺ and CuO_x particles.

3.2.2. UV-vis

UV-vis spectroscopy further examined the existence status of Cu species on Cu_x/CHA. According to previous reports, the band at

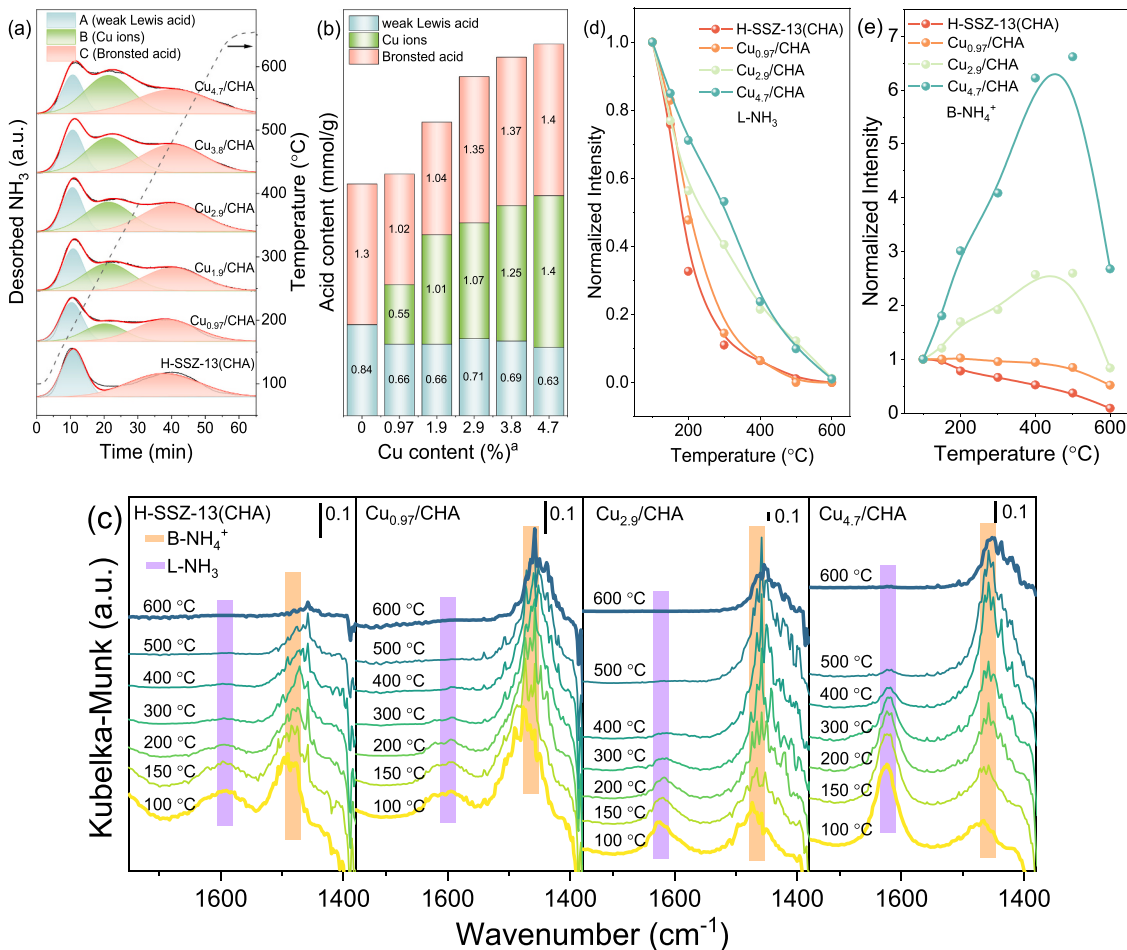


Fig. 4. (a) The NH₃-TPD profiles of H-SSZ-13(CHA) and Cu_x/CHA samples; (b) The acid content of samples obtained by the peak fitting of the results in (a); (c) In situ DRIFTS spectra of Cu_x/CHA during desorption processes, and plot of the intensity of the Lewis acid (d) and Brønsted acid (e) bands on Cu_x/CHA as a function of purge temperature after normalization. (Cu_x/CHA were pretreated in a flow of 1000 ppm NH₃ at 100 °C and then purged with Ar at different temperatures; ^a: Obtained by ICP-OES).

~210 nm was connected to oxygen-to-metal charge transfer, which related to the isolated Cu²⁺ cations (i.e., Z-[Cu(OH)]⁺ and Z₂-Cu²⁺) stabilized in the framework [33,34]. The bands at around 250 nm was related to the charge transfer of Cu in dimeric CuO_x cluster, and 340 nm was connected to the charge transfer of Cu in crystalline CuO_x [35]. There was a board band at around 785 nm that resulted from the d-d transition of oxygen-generated electrons from Cu²⁺ in the out-of-framework CuO_x particles around the twisted octahedron [34, 36].

As shown in Fig. 3(c), for the low Cu content sample (i.e., Cu_{0.97}/CHA), Cu species exist primarily in the form of isolated Cu²⁺ cations in the CHA framework. Moreover, increasing the Cu loadings could increased the bands associated with isolated Cu²⁺ cations and CuO_x species [37], which were consistent with the results of TPR. After normalization (Fig. S6), the bands associated with CuO_x gradually increased with increasing copper content, indicating that higher copper content was favorable for CuO_x species generation, as confirmed in H₂-TPR and STEM.

3.3. Surface adsorption properties of Catalysts

3.3.1. NH₃-TPD

The acidic property played a crucial role in the NH₃-SCR reaction on the Cu zeolites, the effects of Cu content on the acidity of Cu_x/CHA were investigated by NH₃-TPD, and shown in Fig. 4. Two distinct desorption peaks were observed on the resolved curve of H-SSZ-13(CHA), in addition, a new desorption peak (250–350 °C) was found with the introduction of Cu. According to the available studies on NH₃ adsorption on Cu-SSZ-13 zeolite, the peak A at low-temperature (~ 190 °C) was considered to be a weakly adsorbed NH₃ species, which were produced by surface OH groups and extra-framework Al [28,38]. The mid-temperature peak B (250–350 °C) was due to NH₃ adsorption onto the strong Lewis acid sites, which were formed by the isolated Cu²⁺ ions at ion-exchanged sites [39]. The peak C at high-temperature (~ 500 °C) was ascribed to NH₃ adsorption onto the strong Brönsted acid sites [28, 39].

Furthermore, the amount of acid in each desorption peak was calculated by peak area, as shown in Fig. 4(b). For the Cu-containing zeolites (Cu_x/CHA), the acid amount corresponding to B peaks increased with increasing Cu content. The n(NH₃)/n(Cu) ratios were further calculated from the B peak of NH₃-TPD and the ICP-OES results, which are shown in Table S2. The n(NH₃)/n(Cu) ratio in Cu_{0.97}/CHA was 3.6, in the range of 3–4, which is probably due to the fact that the Cu species in Cu_{0.97}/CHA were present in the form of Z-[Cu(OH)]⁺ and Z₂-Cu²⁺. These two copper species could form a four-coordination complexes with three or four NH₃, respectively. It was noteworthy that the n(NH₃)/n(Cu) ratio decreased with increasing Cu content. Combined with the H₂-TPR results, it might be attributed to the increase in Z-[Cu(OH)]⁺ and CuO_x content in the Cu_x/CHA catalysts with increasing copper content. In addition, compared to H-SSZ-13(CHA), the peak C decreased significantly from 1.3 to 1.02 mmol/g in Cu_{0.97}/CHA, indicating that Cu could be in the ion-exchange site, thereby reducing the amount of the Brönsted acid site. In general, the number of Brönsted acid sites in zeolite decreased as the level of ion exchange increased. Combined with the result in Fig. 3, the number of Brönsted acid sites in Cu_x/CHA should decrease with increasing Cu content. However, as the Cu content increased from 0.97 wt% to 4.7 wt%, the acid content of the C peak increased from 1.02 mmol/g to 1.4 mmol/g, which indicated that there might be other reasons for the increase of C peaks.

Moreover, the desorption processes of adsorbed NH₃ species on H-SSZ-13(CHA) and Cu_x/CHA were further examined by *in situ* DRIFTS spectra and are illustrated in Fig. 4(c) and S7. As can be seen, the negative bands at 3800–3500 cm⁻¹ were originated from the stretching vibrations of the O-H bonds which consumed by the adsorption of NH₃ [11]. The bands at 3100–3400 cm⁻¹ and 1400–1700 cm⁻¹ were related to the stretching vibrations and bending vibrations of N-H in adsorbed

NH₃ species, respectively [27]. The bands at 1457–1491 cm⁻¹ correspond to the bending vibrations of N-H in NH₄⁺, which adsorbed on the Brönsted acid sites (B-NH₄⁺) [28]. Whereas, the bands at 1585–1621 cm⁻¹ were derived from the bending vibrations of N-H in the NH₃ which coordinated to the Lewis acid sites (L-NH₃) [27,28].

Fig. 4(d) and (e) plots the variation of the NH₃ adsorbed on the Lewis and Brönsted sites with temperature, respectively. For the Cu-free zeolite, both L-NH₃ and B-NH₄⁺ decreased with increasing purging temperature. In contrast, the Cu-containing zeolites (Cu_x/CHA) exhibited different trends, that is, L-NH₃ monotonically decreased with increasing temperature (Fig. 4(d)), while B-NH₄⁺ first increased and then decreased (Fig. 4(e)). These results demonstrated that an oxolation process (i.e. Z-[Cu(OH)]⁺ + Z₂-Cu²⁺ → Z-[Cu²⁺-O²⁻-Cu²⁺]-Z + Z-H⁺) accompanied by the formation of NH₄⁺ ions (Z-H⁺ + NH₃ → Z-NH₄⁺) was present in Cu_x/CHA during the heating process. The intra-zeolite oxolation process in Cu-SSZ-13 has been proven by Mozgawa et al. [40]. Of note, the NH₄⁺ generation was positively correlated with the Cu content. We further investigated the correlation between the degree of the intra-zeolite oxolation process and the content of Cu species, as depicted in Fig. S8. The results showed that the degree of the intra-zeolite oxolation process was more strongly correlated with the content of Z-[Cu(OH)]⁺ species compared to the content of CuO_x and Z₂-Cu²⁺. This indicated that the higher Z-[Cu(OH)]⁺ species content in Cu_x/CHA, the easier the intra-zeolite oxolation process in Cu_x/CHA could be carried out. Hence, it is reasonable to believe that the intra-zeolite oxolation process was the main reason for the increase of the C peak in NH₃-TPD.

3.3.2. NO_x-TPD

Fig. S9 presents the NO_x-TPD profiles of Cu_x/CHA. All samples showed a weak NO_x desorption peak below 200 °C and an obvious NO_x desorption peak (mainly composed of NO₂) above 300 °C, which were caused by the decomposition of adsorbed nitrite and nitrate species (including thermally stable bridged and bidentate nitrate species), respectively [41,42]. In addition, the NO_x desorption peak of Cu_x/CHA shifted toward higher temperature with increasing Cu content, suggesting that the introduction of Cu promoted higher stability nitrate formation. As shown in Fig. S9(b), the total NO_x desorption of Cu_x/CHA increased from 26.8 to 126.4 μmol/g as the Cu content increased from 0.97 to 4.7 wt%. These results demonstrated that the existence of Cu promoted nitrate species production, which were dependent on the Cu content.

3.4. NH₃-SCR performance

The NO conversion of Cu_x/CHA at reaction temperature between 90 and 650 °C are shown in Fig. 5(a) and S10. Pure H-SSZ-13 catalyst showed poor SCR activity that the NO conversion could not reach 60 % even at 650 °C (Fig. S10(a)). The presence of Cu significantly improved the NH₃-SCR and N₂ selectivity (~ 99 %) over H-SSZ-13. With increasing Cu content from 0.97 wt% to 2.9 wt%, the NO conversion which was above 90 % (T₉₀) of Cu_x/CHA in the low-temperature range decreased from 260 °C to 180 °C. Further increasing Cu content to 4.7 wt%, the T₉₀ increased slightly. However, for the high-temperature activity (> 400 °C) of Cu_x/CHA, the NH₃-SCR activities decreased with the increase of Cu content due to non-selective NH₃ oxidation, which had been demonstrated in previous studies [43]. In addition, N₂O concentration increased with increasing Cu content (Fig. S10(b)).

Furthermore, we also studied the kinetic activation energy (E_a) of the Cu_x/CHA, as shown in Fig. 5(b). The apparent activation energies increased slightly from 26 to 42 kJ/mol with the increase of Cu content (from 0.97 to 4.7 wt%), and a similar trend was found in previous studies [18], which was probably due to the fact that the higher the copper content, the more significant internal diffusion limitation within the zeolite. Moreover, the influence of copper content on the rate in the low-temperature range were investigated and shown in Fig. 5(c). The reaction rate of Cu_x/CHA increased linearly with increasing the Cu

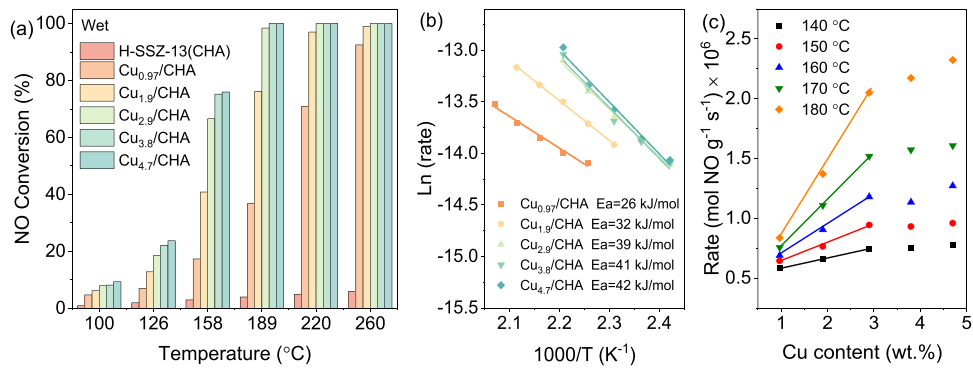


Fig. 5. (a) NO conversion of Cu_x/CHA catalysts; (b) Arrhenius plots for standard SCR in the low-temperature range (< 200 °C) on Cu_x/CHA catalysts; (c) SCR rates as a function of Cu content in different reaction temperatures.

content from 0.97 to 2.9 wt%, whereas it varied nonlinearly when the Cu content was higher than 2.9 wt%. According to the Koros-Nowak criterion, the linear relationship indicated that the reaction was run in the kinetic regime which excludes transfer limitations [44]. Gao et al. [44] also found that the Koros-Nowak criterion hold at moderate Cu contents (0.378 wt% - 3.43 wt%) and that mass-transfer limitations were the primary reason why high Cu content catalysts did not follow the Koros-Nowak criterion. Due to mass-transfer limitations, it is difficult to determine whether a uniform reaction path was followed on Cu_x/CHA from the apparent activation energies alone. Therefore, we

further investigated the effect of Cu content on the reaction mechanism of Cu_x/CHA by using *in situ* DRIFTS.

3.5. *In situ* DRIFTS study of the reaction mechanism

3.5.1. Adsorption of NO_x followed by exposure to NH₃

Fig. 6(a) and S11 demonstrated the NO/O₂ adsorption on the four Cu_x/CHA catalysts at 150 °C. The main adsorbed species of NO_x include bridging nitrate (~1625 cm⁻¹) [45], monodentate nitrate linked to Al sites (~1595 cm⁻¹) [27], monodentate nitrate linked to Cu sites (~

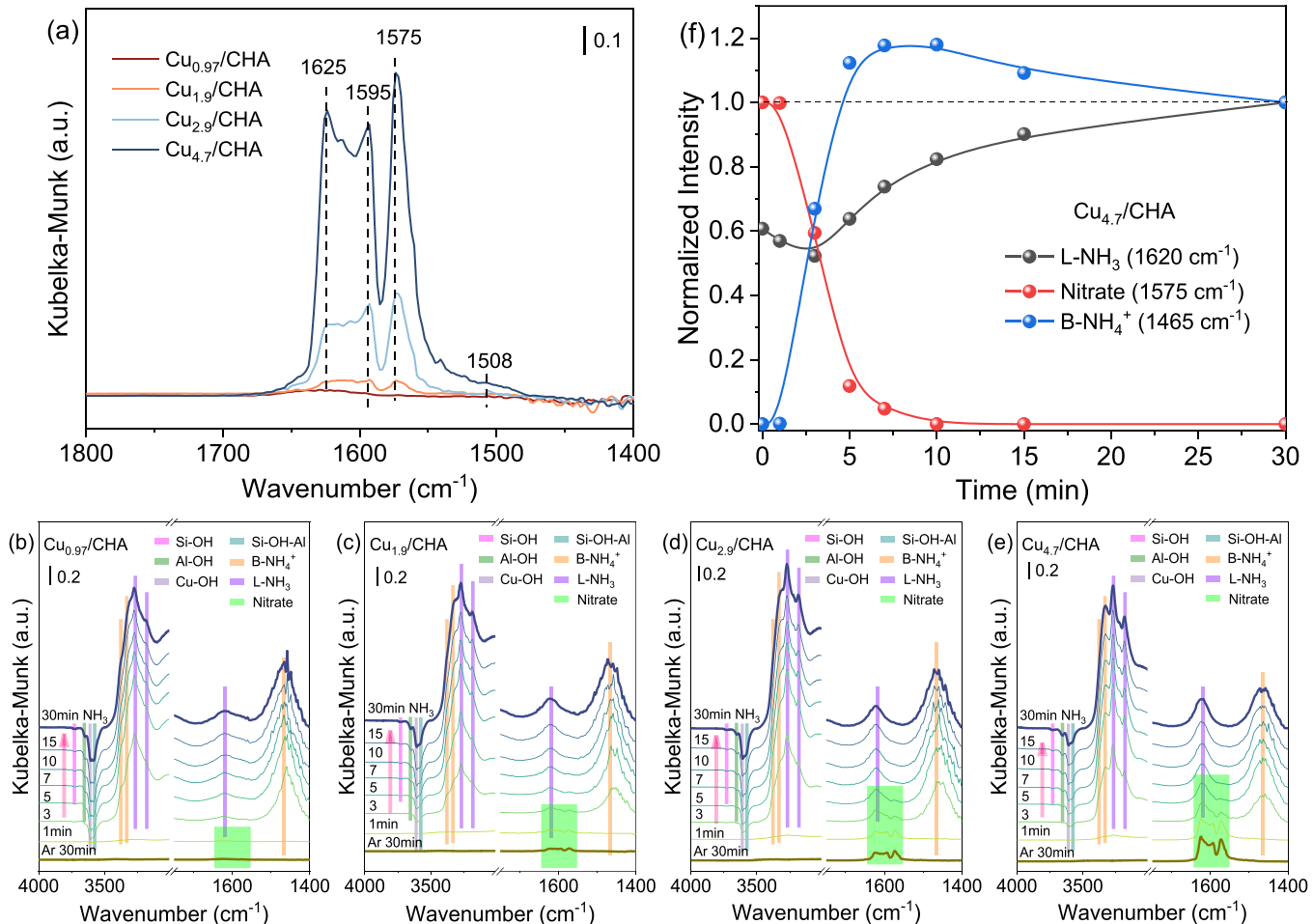


Fig. 6. (a) In situ DRIFTS spectra of Cu_x/CHA at 150 °C in 1000 ppm NO + 5 vol% O₂ atmosphere after 60 min; (b-e) In situ DRIFTS of 1000 ppm NH₃ and pre-adsorbed NO + 5 vol% O₂ species at 150 °C on (b) Cu_{0.97}/CHA, (c) Cu_{1.9}/CHA, (d) Cu_{2.9}/CHA, and (e) Cu_{4.7}/CHA; (f) Normalized band areas associated with the DRIFTS results in Fig. 6(e).

1575 cm^{-1} [28], and NO_2 ($\sim 1508\text{ cm}^{-1}$) [45].

As shown in Fig. S11, the nitrate intensity of Cu_x/CHA increased with increasing $\text{NO}+\text{O}_2$ flux time. In addition, bridging nitrate was formed more readily on catalysts with lower copper content than monodentate nitrate. The nitrate (especially the monodentate nitrates linked to Cu sites) increased remarkably with increasing the content of Cu, suggesting that increasing Cu content was beneficial to produce nitrate species on the catalyst, which was consistent with the results of $\text{NO}+\text{O}_2$ -TPD (Fig. S9). Otherwise, those results demonstrated that although the increase in Cu content enhanced the generation of nitrate, the type of nitrate species on the samples did not change dramatically during the $\text{NO}+\text{O}_2$ adsorption.

The reactions among the NH_3 and adsorbed NO_x species was obtained and shown in Fig. 6(b)-(e). A similar trend was found in all four Cu_x/CHA , i.e., the band strength of the nitrate ($1500\text{--}1700\text{ cm}^{-1}$) decreased rapidly with increasing time of NH_3 introduction, accompanying the forming of adsorbed NH_3 species. To better understand the changes on NO_x species with increasing NH_3 introduction time, the band areas of adsorbed nitrate and NH_3 species on $\text{Cu}_{4.7}/\text{CHA}$ were further normalized, and summarized in Fig. 6(f).

Of note, the band area at 1620 cm^{-1} decreased slightly after 1 min of 1000 ppm NH_3/Ar introduction, while the band area at 1575 cm^{-1} did not change significantly. The absence of the adsorbed NH_3 species bands at this time, suggesting that the decrease at 1620 cm^{-1} might be due to the reaction between adsorbed NO_x species and gas-phase NH_3 , which is

in accordance with the E-R mechanism. After 3 min of introduction of 1000 ppm NH_3/Ar , distinct bands associated with adsorbed NH_3 species were formed. With the formation of adsorbed NH_3 species, the adsorbed nitrate species decreased rapidly until they disappeared completely, which was due to the fact that the adsorbed nitrate species could react with the surface-adsorbed NH_3 , which is in accordance with the L-H mechanism [35]. In addition, the band area of 1620 cm^{-1} decreased and then increased with increasing time of NH_3 introduction, which might be caused by the fact that the spectral bands of both L-NH_3 and nitrate appeared near 1620 cm^{-1} .

Interestingly, the band area at 1465 cm^{-1} first increased and then decreased with increasing NH_3 exposure time. However, to our knowledge, the content of adsorbed NH_3 species increases with adsorption time until adsorption saturation. Therefore, we further investigated the adsorption characteristics of Cu_x/CHA on NH_3 to reveal the intrinsic reason for the decrease in NH_3 adsorption with increasing adsorption time.

3.5.2. Adsorption of NH_3 followed by exposure to NO_x

The adsorption behavior of NH_3 on Cu_x/CHA at $150\text{ }^\circ\text{C}$ was investigated using the *in situ* DRIFTS technique and the results are shown in Fig. 7 and S12. The negative band at $3725, 3654, 3609$, and 3581 cm^{-1} were related to the O-H stretching vibrations of Si-OH, Al-OH, Cu-OH, and Si-OH-Al in the sample, respectively [27,38]. The bands at $3100\text{--}3400\text{ cm}^{-1}$ and $1400\text{--}1700\text{ cm}^{-1}$ were related to the stretching

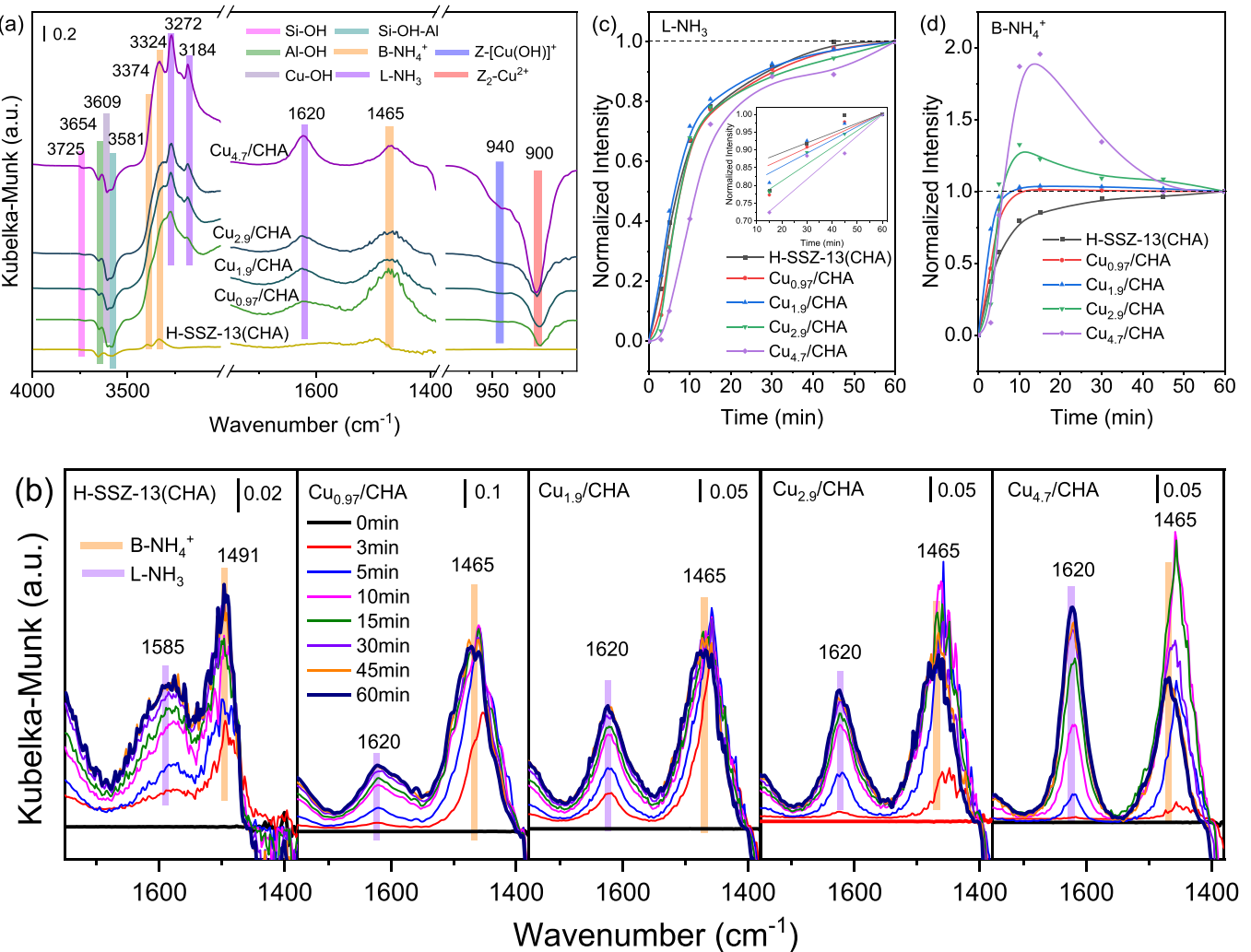


Fig. 7. (a) In situ DRIFTS spectra of Cu_x/CHA at $150\text{ }^\circ\text{C}$ in 1000 ppm NH_3/Ar atmosphere after 60 min. (b) In situ DRIFTS spectra of Cu_x/CHA at $150\text{ }^\circ\text{C}$ in 1000 ppm NH_3/Ar atmosphere. (c) and (d) Normalized band areas associated with (b).

vibrations and bending vibrations of N-H in adsorbed NH_3 species, respectively [27]. As shown in Fig. 7(a) and S12(a), the bands at 3396, 3334, and 1491 cm^{-1} in H-SSZ-13(CHA) were assigned to the bending vibrations of N-H in adsorbed NH_4^+ (B-NH_4^+), while the bands at 1585 cm^{-1} in H-SSZ-13(CHA) was assigned to the bending vibrations of N-H in NH_3 (L-NH_3) [28]. For Cu-containing zeolite (Cu_x/CHA), several new bands were found at 3609, 3272, 3184, 1620, and 1465 cm^{-1} , where those bands at 3272, 3184, and 1620 cm^{-1} were related to the coordinated NH_3 molecule on the isolated Cu^{2+} ions (L-NH_3) [46], while the band at 1465 cm^{-1} was assigned to the adsorbed NH_4^+ on the Brönsted acid sites (B-NH_4^+) [28]. The bands at 940 and 900 cm^{-1} were ascribed to T-O-T vibrations on the Z-Cu(OH)^+ and $\text{Z}_2\text{-Cu}^{2+}$ species, respectively [47].

The trends of NH_3 adsorbed species on H-SSZ-13(CHA) and Cu_x/CHA with increasing NH_3 adsorption time are shown in Fig. 7(b). The peak intensity at 1585 cm^{-1} (L-NH_3) and 1491 cm^{-1} (B-NH_4^+) on H-SSZ-13(CHA) increased significantly in the first 15 min, after that the increasing rate of B-NH_4^+ and L-NH_3 slowed down, but its intensity increased continuously to the near adsorption balance in 60 min. Those results indicated that monotonically increasing trends with the increase of NH_3 adsorption time could reach saturation after 60 min.

Interestingly, for the Cu-containing zeolite (Cu_x/CHA), the adsorbed NH_3 species (especially B-NH_4^+) showed a different trend from that of H-SSZ-13(CHA) as the adsorption time increased. To make this difference in variation clearer, the peak area at $\sim 1620 \text{ cm}^{-1}$ (L-NH_3) and $\sim 1465 \text{ cm}^{-1}$ (B-NH_4^+) after 60 min of adsorption was normalized and the variation of adsorption peak areas with adsorption time are shown in Fig. 7(c) and (d), respectively. The peak area of L-NH_3 on Cu_x/CHA (Fig. 7(c)) increased significantly in the first 15 min, which should be aroused by the rapid adsorption of NH_3 on the isolated Cu^{2+} ions sites. After 15 min, the increasing rate of L-NH_3 slowed down until the adsorption equilibrium was approached at 60 min. In general, B-NH_4^+ should show a similar change to L-NH_3 until adsorption saturation with increasing adsorption time [35]. However, the peak areas of B-NH_4^+ on Cu_x/CHA (Fig. 7(d)) showed different trends, i.e., the peak areas of B-NH_4^+ increased with increasing NH_3 exposing time in the form of a volcano curve, which reached the maximum after adsorption for about 15 min. Notably, after 15 min, the peak areas of B-NH_4^+ did not show the expected increase but rather a decrease, which seems to indicate that part of the B-NH_4^+ was converted to L-NH_3 with increasing adsorption time. In addition, the decreasing trend was more pronounced with the increase in Cu content, which suggested that this trend seemed to be associated with the Cu species in the catalysts and positively correlated with the Cu content.

Among three different Cu species in Cu_x/CHA , the NH_3 was barely adsorbed on CuO_x species (Fig. S13), suggesting that this trend depended on $\text{Z}_2\text{-Cu}^{2+}$ and/or Z-Cu(OH)^+ . Combined with the $\text{H}_2\text{-TPR}$ results, we further investigated the correlation between the degree of

increase in B-NH_4^+ and the content of Cu species, and the results are plotted in Fig. S14. These results indicated that the content of Z-Cu(OH)^+ species was more readily linearly correlated with the degree of increase in B-NH_4^+ than the content of $\text{Z}_2\text{-Cu}^{2+}$ species. Hence, it was reasonable to hypothesize that $\text{Z-Cu(OH)(NH}_3)_x^+$ ($x < 3$) might exhibit analogous properties to B-NH_4^+ , but it will convert to $\text{Z-Cu(OH)(NH}_3)_3^+$ with increasing NH_3 adsorption time and exhibiting more L-NH_3 properties. Based on this conjecture, we also performed DFT theoretical calculations of the NH_3 adsorption process on Z-Cu(OH)^+ and simulated the IR spectra on Z-Cu(OH)^+ with different NH_3 adsorption amounts, the results are shown in Fig. 8 and S15. Two N-H vibrational peaks (α and β) were generated with NH_3 adsorption, and the α peak disappeared when NH_3 adsorption was saturated. These results proved the previous conjecture that $\text{Z-Cu(OH)(NH}_3)_x^+$ ($x < 3$) exhibited not only L-NH_3 properties, but also properties similar to those of B-NH_4^+ . However, when NH_3 adsorption was saturated ($\text{Z-Cu(OH)(NH}_3)_3^+$), it would exhibit more L-NH_3 properties.

Following NH_3 adsorption, the catalyst was purged with argon at 150 °C for 30 min to eliminate physically adsorbed NH_3 , and then a 1000 ppm NO and 5 vol% O_2/Ar gas mixture was introduced. Finally, recorded the spectra and summarized in Fig. 9 and S16–17. With introducing NO + O_2 , the NH_3 adsorbed species ($3100\text{--}3400 \text{ cm}^{-1}$) gradually decreased, and when the exposure time exceeded 45 min, new bands were formed progressively at $1500\text{--}1700 \text{ cm}^{-1}$, which are widely regarded as the surface nitrate or nitro species adsorbed primarily on the Cu species of catalyst [45].

For a better understanding of the trend of NH_3 adsorbed species with NO + O_2 exposure time, the band areas at $\sim 1620 \text{ cm}^{-1}$ (L-NH_3) and $\sim 1465 \text{ cm}^{-1}$ (B-NH_4^+) were normalized to assess the reactivity of NO + O_2 with NH_3 adsorbed at different sites, and plotted in Fig. 9(b) and (c), respectively. For H-SSZ-13, the bands at 1585 cm^{-1} (L-NH_3) and 1491 cm^{-1} (B-NH_4^+) decreased with the introduction of NO and O_2 . Moreover, for Cu-containing zeolite samples, the band areas at 1620 cm^{-1} (L-NH_3) reduced substantially within the first 15 min with introducing NO + O_2 , indicating that adsorbed NH_3 species on the Lewis acid sites (including NH_3 adsorbed at $\text{Z}_2\text{-Cu}^{2+}$ and Z-Cu(OH)^+) could be reacted with the NO/O_2 mixture, and the NH_3 adsorbed on the Z-Cu(OH)^+ has higher reaction performance than that of $\text{Z}_2\text{-Cu}^{2+}$ (as shown in Fig. S17, the decreasing rate of NH_3 on Z-Cu(OH)^+ was greater than that on $\text{Z}_2\text{-Cu}^{2+}$). Following 15 min, the band area of 1620 cm^{-1} increased as the time of introduction of NO + O_2 increased, probably due to the generation of nitrate on the surface.

More interestingly, B-NH_4^+ on Cu_x/CHA increased with increasing NO + O_2 adsorption time, and the increase was more pronounced with higher copper content (Fig. 9(c)). However, there was a simultaneous increase in the intensity of Si-OH-Al (Fig. S16), suggesting that the NH_3 adsorbed on the Brönsted acid sites was released, which should lead to a decrease in B-NH_4^+ . It contradicted the increased intensity of B-NH_4^+ in

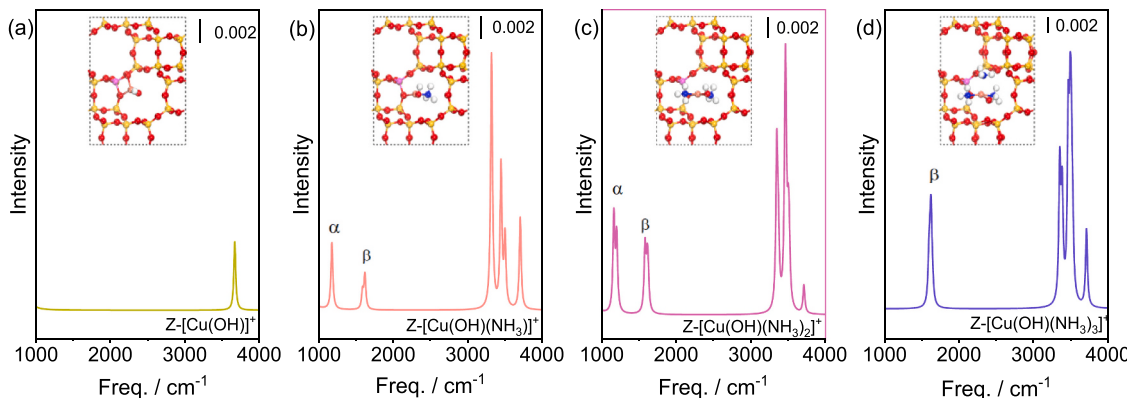


Fig. 8. Infrared vibrational spectra of structural simulations obtained by DFT calculations. (a) Z-Cu(OH)^+ , (b) $\text{Z-Cu(OH)(NH}_3)^+$, (c) $\text{Z-Cu(OH)(NH}_3)_2^+$, (d) $\text{Z-Cu(OH)(NH}_3)_3^+$.

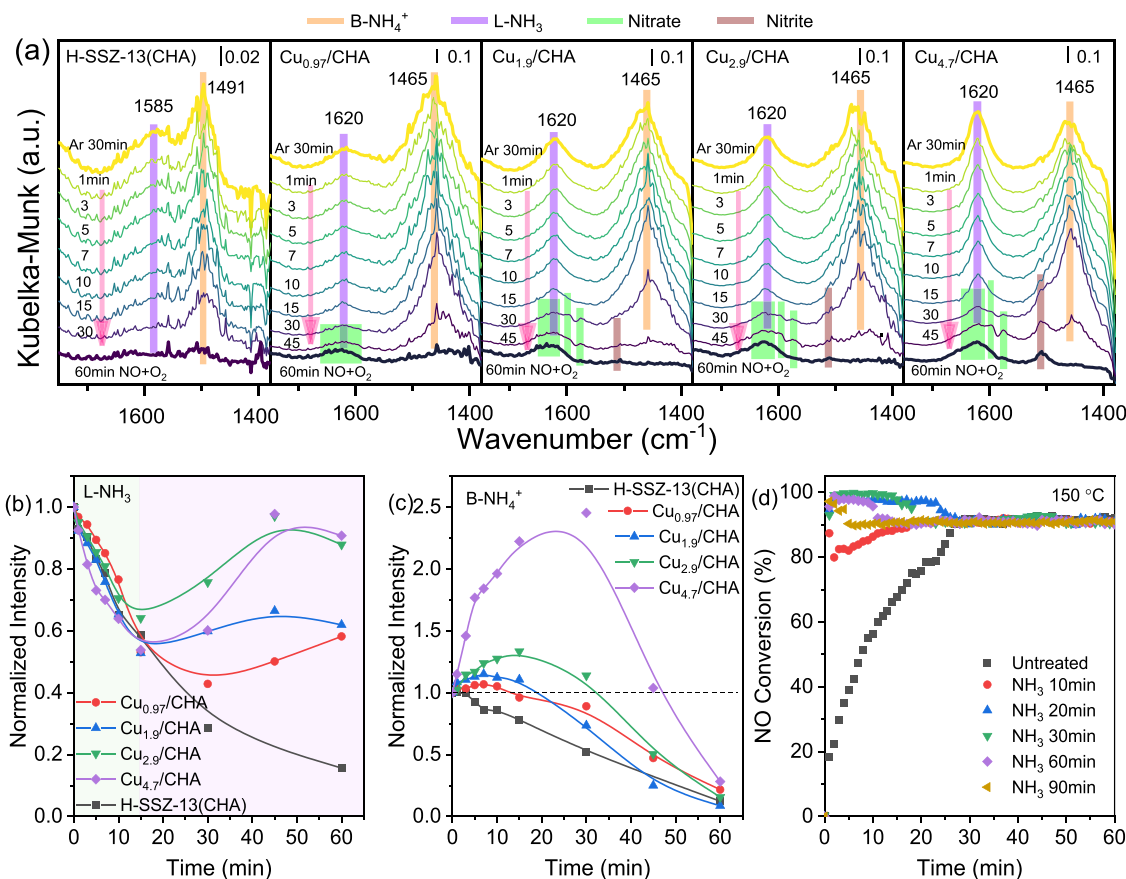


Fig. 9. (a) In situ DRIFTS of 1000 ppm NO + 5 vol% O₂ and pre-adsorbed NH₃ species at 150 °C on Cu_x/CHA samples; (b) and (c) Normalized band areas associated with (a); (d) NH₃-SCR performance of Cu_{4.7}/CHA samples pretreated with different NH₃ adsorption time; Reactant feed contains 500 ppm NO, 500 ppm NH₃, and 5 vol% O₂ balanced with Ar at a weight hourly space velocity (WHSV) of 180,000 mL·h⁻¹·g⁻¹.

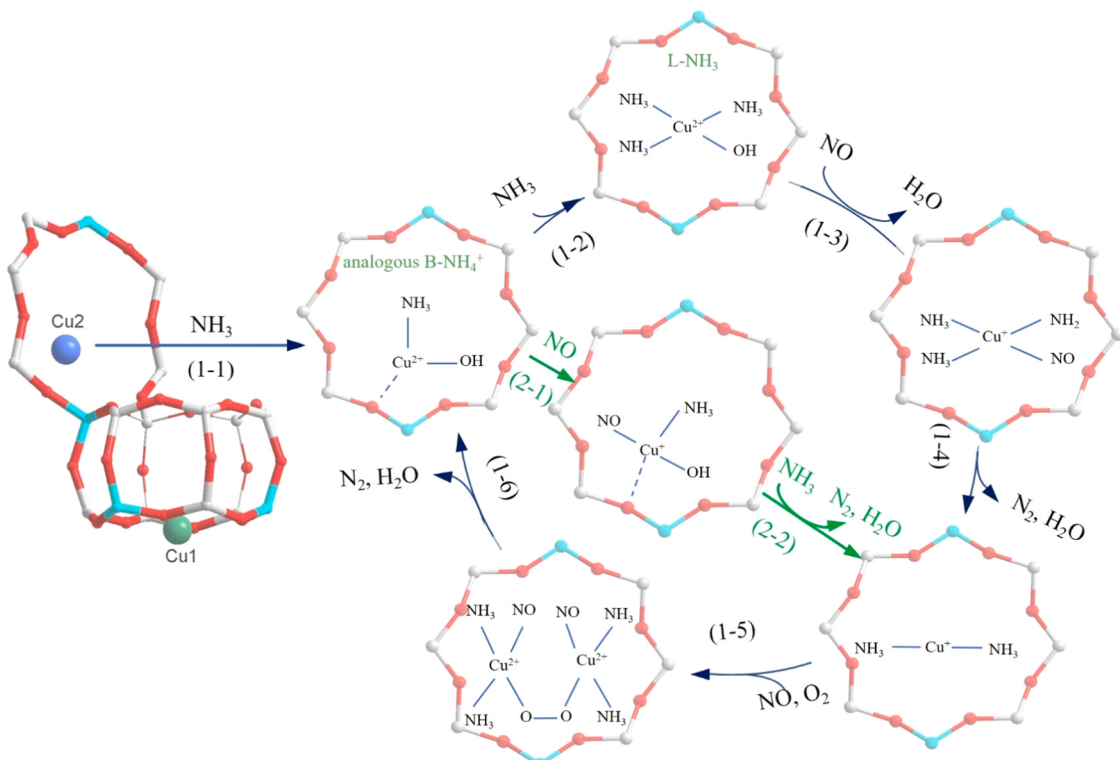


Fig. 10. The possible reaction pathway of the NH₃-SCR cycle at Z-[Cu(OH)]⁺ sites.

Fig. 9(c), demonstrating there were other pathways for the formation of B-NH_4^+ during the reaction, which were closely related to the Cu content.

From the overall reaction, the NH_3 adsorbed at L- and B-acid sites should eventually decrease with the increase of reaction time and reaction temperature. In addition, the B-NH_4^+ had been demonstrated not to be directly involved in the reaction with NO_x , but to supply candidate NH_3 for the Cu site [14]. The increased content of NH_4^+ on the surface during the reaction demonstrated the producing rate of B-NH_4^+ was faster than that of consumption. Paolucci et al. [11] demonstrated by the first-principles thermodynamics and spectroscopies that L- NH_3 species ($\text{Z}_2\text{-Cu}^{2+}$ species) reaction with NO generated new NH_4^+ species (see steps (1–3) in Fig. S18). On the other hand, as shown in the NH_3 adsorption process (Fig. 7), we found that the unsaturated adsorbed $\text{Z-}[\text{Cu(OH)}]^+$ species ($\text{Z-}[\text{Cu(OH)}(\text{NH}_3)_x]^+ (x<3)$) exhibited properties similar to those of B-NH_4^+ , which led to an increase in B-NH_4^+ . To verify which Cu species were responsible for this phenomenon, we investigated the correlation between the degree of B-NH_4^+ increase during the reaction and the content of Cu species (Fig. S19). The results showed that the correlation between the degree of B-NH_4^+ increase during the reaction and the $\text{Z-}[\text{Cu(OH)}]^+$ species was higher than that of $\text{Z}_2\text{-Cu}^{2+}$ species. Therefore, part of the increase in B-NH_4^+ came from $\text{Z-}[\text{Cu(OH)}]^+$, which were caused by the reaction of saturated adsorbed $\text{Z-}[\text{Cu(OH)}(\text{NH}_3)_3]^+$ species with $\text{NO} + \text{O}_2$ to produce unsaturated adsorbed $\text{Z-}[\text{Cu(OH)}(\text{NH}_3)_x]^+ (x<3)$ species (following steps (1–3)-(1–6) in Fig. 10).

For Cu_x/CHA , there were three main Cu species, $\text{Z}_2\text{-Cu}^{2+}$, $\text{Z-}[\text{Cu(OH)}]^+$, and CuO_x . It was generally believed that $\text{Z-}[\text{Cu(OH)}]^+$ had higher low-temperature reactivity and that pairs of NH_3 -solvated Cu species dynamically combine to form NH_3 -SCR active sites at low temperatures [11,18,20]. However, in fact, as mentioned above, different NH_3 coordination numbers on $\text{Z-}[\text{Cu(OH)}]^+$ could exhibit different properties, which directly affect the reaction performance of the catalyst. Hence, it was reasonable to believe that not only the content of $\text{Z-}[\text{Cu(OH)}]^+$ species, but also the degree of NH_3 coordination of $\text{Z-}[\text{Cu(OH)}]^+$ species affect the performance of the low-temperature NH_3 -SCR reaction. To prove this conjecture, we investigated the effect of different NH_3 pre-adsorption times on the NH_3 -SCR performance of $\text{Cu}_{4.7}/\text{CHA}$ samples, and the results are shown in Fig. 9(d) and S20. After NH_3 pre-adsorption, the NO conversion of the $\text{Cu}_{4.7}/\text{CHA}$ samples was significantly increased, especially in the first 30 min, indicating that the catalysts after NH_3 pre-adsorption had higher NH_3 -SCR reaction performance than the untreated catalysts. However, with the increase of NH_3 pre-adsorption time, the NO conversion first increased and then decreased, indicating a decrease in activity after saturation of NH_3 adsorption. Those results suggested that the unsaturated adsorbed species ($\text{Z-}[\text{Cu(OH)}(\text{NH}_3)_x]^+ (x<3)$) probably exhibited higher reaction performance than saturated adsorbed $\text{Z-}[\text{Cu(OH)}(\text{NH}_3)_3]^+$ species (following steps (2–1)-(2–2) in Fig. 10). This provided a new idea to improve the catalyst conversion in practical applications (cold start) by pre-adsorbing NH_3 to ensure that NO reacted quickly.

Furthermore, the application of the reaction mechanism depended mainly on the catalyst systems and the reaction conditions, for example, the reaction gas composition and reaction temperature [48,49]. In this work, for the Cu_x/CHA catalyst, as shown in Figs. 6 and 9, the NH_3 -SCR reaction process in the low-temperature region followed both the L-H mechanism (the adsorbed NH_3 species react with the adsorbed NO_x species) and the E-R mechanism (the adsorbed NH_3 species react with the gaseous NO_x), as illustrated in Fig. 10.

4. Conclusions

In this work, the Al-rich Cu_x/CHA catalysts were prepared by the IWI method, and the NH_3 -SCR performance, NH_3 dissolution process and NH_3 -SCR catalytic mechanism of Cu active sites were investigated. The Al-rich Cu_x/CHA catalysts showed high NO conversion and N_2 selectivity, and the NO conversion increased with increasing the Cu content. Characterization results showed that the $\text{Z-}[\text{Cu(OH)}]^+$ content in the

Cu_x/CHA samples gradually increased with the increase of copper content, which improved the low-temperature activity of the Cu_x/CHA samples. The $\text{Z}_2\text{-Cu}^{2+}$ content increased first and then changed insignificantly. At Cu contents higher than 1.9 wt%, CuO_x species were produced, which lead to a decrease in the high-temperature activity of Cu_x/CHA . And the higher the Cu content, the higher the content of CuO_x species. These results suggested that high Cu content promoted the formation of $\text{Z-}[\text{Cu(OH)}]^+$ and CuO_x particles. In addition, the high Cu content not only improved the adsorption capacity of NO_x but also increased the intra-zeolite oxolation process in the Cu_x/CHA catalysts, which led to an increase in the acid content associated with the Brønsted acid sites in the NH_3 -TPD with the increase of Cu content. *In situ* DRIFTS were utilized to detect the adsorption and reaction properties of the Cu_x/CHA catalysts on the reactants and to investigate the reaction mechanism. The results suggested that the $\text{Z-}[\text{Cu(OH)}(\text{NH}_3)_x]^+ (x<3)$ might exhibit analogous properties to B-NH_4^+ , but it will convert to $\text{Z-}[\text{Cu(OH)}(\text{NH}_3)_3]^+$ with increasing NH_3 adsorption time and exhibit more L- NH_3 properties. Moreover, not only the content, but also the degree of NH_3 coordination of $\text{Z-}[\text{Cu(OH)}]^+$ species affects the performance of the low-temperature NH_3 -SCR reaction. Those finds might provide a new insight into understanding the role of B-NH_4^+ in low-temperature reactions.

CRediT authorship contribution statement

Yali Shen: Writing – original draft, Methodology, Investigation, Data curation, Conceptualization. **Zhiqiang Wang:** Software, Investigation, Formal analysis. **Shasha Ge:** Methodology, Investigation. **Li Wang:** Validation, Methodology. **Wangcheng Zhan:** Visualization, Funding acquisition. **Qiguang Dai:** Visualization, Validation. **Yanglong Guo:** Resources, Project administration. **Yun Guo:** Writing – review & editing, Supervision. **Aiyong Wang:** Writing – review & editing, Supervision.

Declaration of Competing Interest

The authors declare that they have no known competing financial interests or personal relationships that could have appeared to influence the work reported in this paper.

Data availability

Data will be made available on request.

Acknowledgements

This work was supported by the National Key Research and Development Program of China (2023YFA1508500), the National Natural Science Foundation of China (22106101, U21A20326), and the Fundamental Research Funds for the Central Universities.

Appendix A. Supporting information

Supplementary data associated with this article can be found in the online version at doi:10.1016/j.apcatb.2024.124094.

References

- [1] Y. Wu, W. Zhao, S.H. Ahn, Y. Wang, E.D. Walter, Y. Chen, M.A. Derewinski, N. M. Washton, K.G. Rappe, Y. Wang, D. Mei, S.B. Hong, F. Gao, Interplay between copper redox and transfer and support acidity and topology in low temperature NH_3 -SCR, Nat. Commun. 14 (2023) 2633, <https://doi.org/10.1038/s41467-023-38309-8>.
- [2] Y. Shan, G. He, J. Du, Y. Sun, Z. Liu, Y. Fu, F. Liu, X. Shi, Y. Yu, H. He, Strikingly distinctive NH_3 -SCR behavior over Cu-SSZ-13 in the presence of NO_2 , Nat. Commun. 13 (2022) 4606, <https://doi.org/10.1038/s41467-022-32136-z>.
- [3] T. Andana, K.G. Rappé, N.C. Nelson, F. Gao, Y. Wang, Selective catalytic reduction of NO_x with NH_3 over Ce-Mn oxide and Cu-SSZ-13 composite catalysts – low

- temperature enhancement, *Appl. Catal. B: Environ.* (2022) 121522, <https://doi.org/10.1016/j.apcatb.2022.121522>.
- [4] X. Ye, J.E. Schmidt, R.P. Wang, I.K. van Ravenhorst, R. Oord, T. Chen, F. de Groot, F. Meirer, B.M. Weckhuysen, Deactivation of Cu-exchanged automotive-emission NH₃-SCR catalysts elucidated with nanoscale resolution using scanning transmission X-ray microscopy, *Angew. Chem. Int. Ed.* 59 (2020) 15610–15617, <https://doi.org/10.1002/anie.201916554>.
 - [5] B. Peng, K.G. Rappé, Y. Cui, F. Gao, J. Szanyi, M.J. Olszta, E.D. Walter, Y. Wang, J. D. Holladay, R.A. Goffe, Enhancement of high-temperature selectivity on Cu-SSZ-13 towards NH₃-SCR reaction from highly dispersed ZrO₂, *Appl. Catal. B: Environ.* 263 (2020) 118359, <https://doi.org/10.1016/j.apcatb.2019.118359>.
 - [6] D. Chen, Y. Yan, A. Guo, V. Rizzotto, H. Lei, Z. Qiao, H. Liang, M. Jabłońska, X. Jiang, J. Jiang, R. Palkovits, P. Chen, D. Ye, U. Simon, Mechanistic insights into the promotion of low-temperature NH₃-SCR catalysis by copper auto-reduction in Cu-zeolites, *Appl. Catal. B: Environ.* 322 (2023) 122118, <https://doi.org/10.1016/j.apcatb.2022.122118>.
 - [7] V.V. Mesilov, S.L. Bergman, S. Dahlin, Y. Xiao, S. Xi, M. Zhirui, L. Xu, W. Chen, L. J. Pettersson, S.L. Bernasek, Differences in oxidation-reduction kinetics and mobility of Cu species in fresh and SO₂-poisoned Cu-SSZ-13 catalysts, *Appl. Catal. B: Environ.* 284 (2021) 119756, <https://doi.org/10.1016/j.apcatb.2020.119756>.
 - [8] L. Chen, T.V.W. Janssens, P.N.R. Venneström, J. Jansson, M. Skoglundh, H. Grönbeck, A complete multisite reaction mechanism for low-temperature NH₃-SCR over Cu-CHA, *ACS Catal.* 10 (2020) 5646–5656, <https://doi.org/10.1021/acscatal.0c00440>.
 - [9] R. Daya, D.J. Deka, A. Goswami, U. Menon, D. Trandal, W.P. Partridge, S.Y. Joshi, A redox model for NO oxidation, NH₃ oxidation and high temperature standard SCR over Cu-SSZ-13, *Appl. Catal. B: Environ.* 328 (2023) 122524, <https://doi.org/10.1016/j.apcatb.2023.122524>.
 - [10] Y. Cui, Y. Wang, E.D. Walter, J. Szanyi, Y. Wang, F. Gao, Influences of Na⁺ co-cation on the structure and performance of Cu/SSZ-13 selective catalytic reduction catalysts, *Catal. Today* 339 (2020) 233–240, <https://doi.org/10.1016/j.cattod.2019.02.037>.
 - [11] C. Paolucci, A.A. Parekh, I. Khurana, J.R. Di Iorio, H. Li, J.D. Albarraín Caballero, A.J. Shih, T. Anggara, W.N. Delgass, J.T. Miller, F.H. Ribeiro, R. Gounder, W. F. Schneider, Catalysis in a cage: condition-dependent speciation and dynamics of exchanged Cu cations in SSZ-13 zeolites, *J. Am. Chem. Soc.* 138 (2016) 6028–6048, <https://doi.org/10.1021/jacs.6b02651>.
 - [12] K.A. Lomachenko, E. Borfecchia, C. Negri, G. Berlier, C. Lamberti, P. Beato, H. Falsig, S. Bordiga, The Cu-CHA deNO_x catalyst in action: Temperature-dependent NH₃-assisted selective catalytic reduction monitored by operando XAS and XES, *J. Am. Chem. Soc.* 138 (2016) 12025–12028, <https://doi.org/10.1021/jacs.6b06809>.
 - [13] L. Ren, L. Zhu, C. Yang, Y. Chen, Q. Sun, H. Zhang, C. Li, F. Nawaz, X. Meng, F. S. Xiao, Designed copper-amine complex as an efficient template for one-pot synthesis of Cu-SSZ-13 zeolite with excellent activity for selective catalytic reduction of NO_x by NH₃, *Chem. Commun.* 47 (2011) 9789–9791, <https://doi.org/10.1039/c1cc12469b>.
 - [14] F. Gao, N.M. Washton, Y. Wang, M. Kollár, J. Szanyi, C.H.F. Peden, Effects of Si/Al ratio on Cu-SSZ-13 NH₃-SCR catalysts: implications for the active Cu species and the roles of Brønsted acidity, *J. Catal.* 331 (2015) 25–38, <https://doi.org/10.1016/j.jcat.2015.08.004>.
 - [15] S.L. Bergman, S. Dahlin, V.V. Mesilov, Y. Xiao, J. Englund, S. Xi, C. Tang, M. Skoglundh, L.J. Pettersson, S.L. Bernasek, In-situ studies of oxidation/reduction of copper in Cu-CHA SCR catalysts: comparison of fresh and SO₂-poisoned catalysts, *Appl. Catal. B: Environ.* 269 (2020) 118722, <https://doi.org/10.1016/j.apcatb.2020.118722>.
 - [16] D.J. Deka, R. Daya, A. Ladshaw, D. Trandal, S.Y. Joshi, W.P. Partridge, Assessing impact of real-world aging on Cu-redox half cycles of a Cu-SSZ-13 SCR catalyst via transient response measurements and kinetic modeling, *Appl. Catal. B: Environ.* 309 (2022) 121233, <https://doi.org/10.1016/j.apcatb.2022.121233>.
 - [17] A. Guo, K. Xie, H. Lei, V. Rizzotto, L. Chen, M. Fu, P. Chen, Y. Peng, D. Ye, U. Simon, Inhibition effect of phosphorus poisoning on the dynamics and redox of Cu active sites in a Cu-SSZ-13 NH₃-SCR catalyst for NO_x reduction, *Environ. Sci. Technol.* 55 (2021) 12619–12629, <https://doi.org/10.1021/acs.est.1c03630>.
 - [18] F. Gao, D. Mei, Y. Wang, J. Szanyi, C.H.F. Peden, Selective catalytic reduction over Cu/SSZ-13: Linking homo- and heterogeneous catalysis, *J. Am. Chem. Soc.* 139 (2017) 4935–4942, <https://doi.org/10.1021/jacs.7b01128>.
 - [19] R. Daya, D. Trandal, R.K. Dadi, H. Li, S.Y. Joshi, J. Luo, A. Kumar, A. Yezersets, Kinetics and thermodynamics of ammonia solvation on Z₂Cu, ZCuOH and ZCu sites in Cu-SSZ-13 – Implications for hydrothermal aging, *Appl. Catal. B: Environ.* 297 (2021) 120444, <https://doi.org/10.1016/j.apcatb.2021.120444>.
 - [20] C. Paolucci, I. Khurana, A.A. Parekh, S. Li, A.J. Shih, H. Li, J.R.D. Iorio, J. D. Albarraín-Caballero, A. Yezersets, J.T. Miller, W.N. Delgass, F.H. Ribeiro, W. F. Schneider, R. Gounder, Dynamic multinuclear sites formed by mobilized copper ions in NO_x selective catalytic reduction, *Science* 357 (2017) 898–903, <https://doi.org/10.1126/science.aan5630>.
 - [21] H. Lei, D. Chen, J.-y Yang, A. Khetan, J. Jiang, B. Peng, U. Simon, D. Ye, P. Chen, Revealing the formation and reactivity of cage-confined Cu pairs in catalytic NO_x reduction over Cu-SSZ-13 zeolites by in situ UV–Vis spectroscopy and time-dependent DFT calculation, *Environ. Sci. Technol.* 57 (2023) 12465–12475, <https://doi.org/10.1021/acs.est.3c00458>.
 - [22] Y. Zhang, J. Zhang, H. Wang, W. Yang, C. Wang, Y. Peng, J. Chen, J. Li, F. Gao, Selective catalytic reduction of NO_x with NH₃ over Cu/SSZ-13: Elucidating dynamics of Cu active sites with in situ UV–Vis spectroscopy and DFT calculations, *J. Phys. Chem. C* 126 (2022) 8720–8733, <https://doi.org/10.1021/acs.jpcc.2c01268>.
 - [23] H. Lee, I. Song, S.W. Jeon, D.H. Kim, Mobility of Cu ions in Cu-SSZ-13 determines the reactivity of selective catalytic reduction of NO_x with NH₃, *J. Phys. Chem. Lett.* 12 (2021) 3210–3216, <https://doi.org/10.1021/acs.jpclett.1c00181>.
 - [24] N.D. Nasello, N. Usberti, U. Iacobone, F. Gramigni, W. Hu, S. Liu, I. Nova, X. Gao, E. Tronconi, Dual-site RHC and OHC transient kinetics predict Low-T standard SCR steady-state rates over a Cu-CHA catalyst, *ACS Catal.* 13 (2023) 2723–2734, <https://doi.org/10.1021/acscatal.2c06071>.
 - [25] W. Hu, T. Selleri, F. Gramigni, E. Fenes, K.R. Rout, S. Liu, I. Nova, D. Chen, X. Gao, E. Tronconi, On the redox mechanism of Low-Temperature NH₃-SCR over Cu-CHA: A combined experimental and theoretical study of the reduction half cycle, *Angew. Chem. Int. Ed.* 60 (2021) 7197–7204, <https://doi.org/10.1002/anie.202014926>.
 - [26] D. Chen, A. Khetan, H. Lei, V. Rizzotto, J.-Y. Yang, J. Jiang, Q. Sun, B. Peng, P. Chen, R. Palkovits, D. Ye, U. Simon, Copper site motion promotes catalytic NO_x reduction under zeolite confinement, *Environ. Sci. Technol.* 57 (2023) 16121–16130, <https://doi.org/10.1021/acs.est.3c03422>.
 - [27] Y. Shen, T. Li, J. Yang, A. Wang, L. Wang, W. Zhan, Y. Guo, Y. Guo, Enhanced low-temperature performance of Al-rich Cu-SSZ-13 by Ce modification upon hydrothermal aging for NH₃-SCR, *Chem. Eng. J.* 473 (2023) 145275, <https://doi.org/10.1016/j.cej.2023.145275>.
 - [28] Y. Shen, W. Dong, L. Zhang, L. Wang, B. Chen, Y. Guo, W. Zhan, A. Wang, C. Ge, Y. Guo, Revealing the mechanism of K-enhanced Cu-SSZ-13 catalysts against hydrothermal aging and P-poisoning for NO_x reduction by NH₃-SCR, *Sep. Purif. Technol.* 330 (2024) 125248, <https://doi.org/10.1016/j.seppur.2023.125248>.
 - [29] F. Gao, M. Kollár, R.K. Kukkadapu, N.M. Washton, Y. Wang, J. Szanyi, C.H. F. Peden, Fe/SSZ-13 as an NH₃-SCR catalyst: a reaction kinetics and FTIR/Mössbauer spectroscopic study, *Appl. Catal. B: Environ.* 164 (2015) 407–419, <https://doi.org/10.1016/j.apcatb.2014.09.031>.
 - [30] E. Borfecchia, P. Beato, S. Svelle, U. Olsbye, C. Lamberti, S. Bordiga, Cu-CHA - a model system for applied selective redox catalysis, *Chem. Soc. Rev.* 47 (2018) 8097–8133, <https://doi.org/10.1039/c8cs00373d>.
 - [31] J. Hun Kwak, H. Zhu, J.H. Lee, C.H. Peden, J. Szanyi, Two different cationic positions in Cu-SSZ-13? *Chem. Commun.* 48 (2012) 4758–4760, <https://doi.org/10.1039/c2cc31184d>.
 - [32] R. Yu, Z. Zhao, S. Huang, W. Zhang, Cu-SSZ-13 zeolite-metal oxide hybrid catalysts with enhanced SO₂-tolerance in the NH₃-SCR of NO_x, *Appl. Catal. B: Environ.* 269 (2020) 118825, <https://doi.org/10.1016/j.apcatb.2020.118825>.
 - [33] K.A. Tarach, M. Jabłońska, K. Pyra, M. Liebau, B. Reiprich, R. Gläser, K. Góra-Marek, Effect of zeolite topology on NH₃-SCR activity and stability of Cu-exchanged zeolites, *Appl. Catal. B: Environ.* 284 (2021) 119752, <https://doi.org/10.1016/j.apcatb.2020.119752>.
 - [34] C. Fan, Z. Chen, L. Pang, S. Ming, C. Dong, K. Brou Albert, P. Liu, J. Wang, D. Zhu, H. Chen, T. Li, Steam and alkali resistant Cu-SSZ-13 catalyst for the selective catalytic reduction of NO_x in diesel exhaust, *Chem. Eng. J.* 334 (2018) 344–354, <https://doi.org/10.1016/j.cej.2017.09.181>.
 - [35] J. Zhang, J. Liang, H. Peng, Y. Mi, P. Luo, H. Xu, M. He, P. Wu, Cost-effective fast-synthesis of chabazite zeolites for the reduction of NO_x, *Appl. Catal. B: Environ.* 292 (2021) 120163, <https://doi.org/10.1016/j.apcatb.2021.120163>.
 - [36] Z. Chen, L. Liu, H. Qu, B. Zhou, H. Xie, Q. Zhong, Migration of cations and shell functionalization for Cu-Ce-La/SSZ-13@ZSM-5: the contribution to activity and hydrothermal stability in the selective catalytic reduction reaction, *J. Catal.* 392 (2020) 217–230, <https://doi.org/10.1016/j.jcat.2020.10.005>.
 - [37] L. Negahdar, N.E. Omori, M.G. Quesne, M.D. Frogley, F. Cacho-Nerin, W. Jones, S. W.T. Price, C.R.A. Catlow, A.M. Beale, Elucidating the significance of copper and nitrate speciation in Cu-SSZ-13 for N₂O formation during NH₃-SCR, *ACS Catal.* 11 (2021) 13091–13101, <https://doi.org/10.1021/acscatal.1c03174>.
 - [38] H. Jiang, B. Guan, H. Lin, Z. Huang, Cu/SSZ-13 zeolites prepared by in situ hydrothermal synthesis method as NH₃-SCR catalysts: influence of the Si/Al ratio on the activity and hydrothermal properties, *Fuel* 255 (2019) 115587, <https://doi.org/10.1016/j.fuel.2019.05.170>.
 - [39] A. Wang, M. Elena Azzoni, J. Han, K. Xie, L. Olsson, Insight into the effect of phosphorus poisoning of Cu/zeolites with different framework towards NH₃-SCR, *Chem. Eng. J.* 454 (2023) 140040, <https://doi.org/10.1016/j.cej.2022.140040>.
 - [40] B. Mozgawa, F. Zasada, M. Fedyna, K. Gora-Marek, E. Tabor, K. Mlekodaj, J. Dedecek, Z. Zhao, P. Pietrzky, Z. Sojka, Analysis of NH₃-TPD profiles for CuSSZ-13 SCR catalyst of controlled Al distribution - complexity resolved by first principles thermodynamics of NH₃ desorption, IR and EPR insight into Cu speciation, *Chem. – A Eur. J.* 27 (2021) 17159–17180, <https://doi.org/10.1002/chem.202102790>.
 - [41] Q. Xu, Z. Fang, Y. Chen, Y. Guo, L. Wang, Y. Wang, J. Zhang, W. Zhan, Titania-samarium-manganese composite oxide for the low-temperature selective catalytic reduction of NO with NH₃, *Environ. Sci. Technol.* 54 (2020) 2530–2538, <https://doi.org/10.1021/acs.est.9b06701>.
 - [42] L. Ma, Y. Cheng, G. Cavataio, R.W. McCabe, L. Fu, J. Li, Characterization of commercial Cu-SSZ-13 and Cu-SAPO-34 catalysts with hydrothermal treatment for NH₃-SCR of NO_x in diesel exhaust, *Chem. Eng. J.* 225 (2013) 323–330, <https://doi.org/10.1016/j.cej.2013.03.078>.
 - [43] F. Gao, E.D. Walter, E.M. Karp, J. Luo, R.G. Tonkyn, J.H. Kwak, J. Szanyi, C.H. F. Peden, Structure–activity relationships in NH₃-SCR over Cu-SSZ-13 as probed by reaction kinetics and EPR studies, *J. Catal.* 300 (2013) 20–29, <https://doi.org/10.1016/j.jcat.2012.12.020>.
 - [44] F. Gao, E.D. Walter, M. Kollar, Y. Wang, J. Szanyi, C.H.F. Peden, Understanding ammonia selective catalytic reduction kinetics over Cu/SSZ-13 from motion of the Cu ions, *J. Catal.* 319 (2014) 1–14, <https://doi.org/10.1016/j.jcat.2014.08.010>.
 - [45] W. Su, H. Chang, Y. Peng, C. Zhang, J. Li, Reaction pathway investigation on the selective catalytic reduction of NO with NH₃ over Cu/SSZ-13 at low temperatures, *Environ. Sci. Technol.* 49 (2015) 467–473, <https://doi.org/10.1021/es503430w>.

- [46] B. Jiang, S. Zhao, Y. Wang, Y. Wenren, Z. Zhu, J. Harding, X. Zhang, X. Tu, X. Zhang, Plasma-enhanced low temperature NH₃-SCR of NO_x over a Cu-Mn/SAPO-34 catalyst under oxygen-rich conditions, *Appl. Catal. B: Environ.* 286 (2021) 119886, <https://doi.org/10.1016/j.apcatb.2021.119886>.
- [47] A. Wang, L. Olsson, Insight into the SO₂ poisoning mechanism for NO_x removal by NH₃-SCR over Cu/LTA and Cu/SSZ-13, *Chem. Eng. J.* 395 (2020) 125048, <https://doi.org/10.1016/j.cej.2020.125048>.
- [48] C. Negri, T. Selleri, E. Borfecchia, A. Martini, K.A. Lomachenko, T.V.W. Janssens, M. Cutini, S. Bordiga, G. Berlier, Structure and reactivity of oxygen-bridged diamino dicopper(II) complexes in Cu-ion-exchanged chabazite catalyst for NH₃-mediated selective catalytic reduction, *J. Am. Chem. Soc.* 142 (2020) 15884–15896, <https://doi.org/10.1021/jacs.0c06270>.
- [49] Y. Xin, Q. Li, Z. Zhang, Zeolitic materials for DeNO_x selective catalytic reduction, *ChemCatChem* 10 (2018) 29–41, <https://doi.org/10.1002/cctc.201700854>.